Numerical Investigation of Wall Heat Conduction Effects in Catalytic Combustion Systems

Undergraduate Honors Thesis

By

Michael Grimm

Department of Mechanical Engineering

The Ohio State University,

Columbus, OH 43210, USA

Advisor: Dr. Sandip Mazumder

Department of Mechanical Engineering

The Ohio State University

February 2007

ABSTRACT

Catalytic converters are used in a variety of applications ranging from low-temperature combustion for gas turbine applications to the removal of pollutants from engine exhaust flow. Catalytic converters currently used in industry consist of a ceramic monolithic plug. This monolithic plug has a honeycomb-like structure, and is comprised of many small cylindrical channels (tubes), the inner surfaces of which are covered with a reactive catalyst. Determining the effect of the thermal conductivity of the monolith ceramic material on the ignition, flame stability, and steady state combustion will provide a scientific foundation with regard to the selection of materials for the construction of catalytic monoliths. This effect is investigated in this study through numerical simulations. Two commonly used materials are compared: cordierite, a ceramic with a low thermal conductivity, and silicon carbide, a ceramic with a high thermal conductivity.

Another issue that is critical to the design of a catalytic converter is the length of the monolith plug. The optimum length of a monolith tube is one that completely converts the incoming flow while utilizing the entire length of the catalytic coating. In practice, the length is adjusted by stacking monolith plugs end-to-end, though it is unclear how different the end-to-end plugs are when compared to a single continuous tube of the same length. This study numerically investigates the effects of this practice, with the goal to determine if a tube of length $2L$ exhibits the same behavior as two identical tube sections placed end-to-end, each of length L.

The commercial CFD software *CFD-ACE+*™ was utilized to investigate the afore-stated issues. The inlet flow rates of the methane-air mixture and the fuel equivalence ratio (or fuel-air ratio) were treated as parameters. Only lean and stoichiometric mixtures were considered because in practice catalytic combustion is not performed with rich mixtures. Catalytic

combustion of a methane-air mixture on a platinum catalyst was used as the candidate system because the chemistry of this system is well documented. The models were set up and tested in an order of increasing complexity to ensure steady progress in the research. Beginning with simple flow and heat transfer, the model was extended to include a single step combustion reaction, and finally a detailed reaction mechanism consisting of 24 surface reactions between 19 species. Both steady-state and transient simulations were conducted.

The results show that thermal conductivity of the ceramic monolith has a large effect on ignition, flame stability, and steady state combustion. The ceramic material with a high thermal conductivity value, namely silicon carbide, produces a stable flame over a much wider range of inlet flow rates than the ceramic material with a low thermal conductivity value, namely cordierite. Over their respective ranges of ignition, for both silicon carbide and cordierite, the maximum temperature of the monolith tube is more or less the same, indicating that there is no effect of thermal conductivity on the maximum temperature. Therefore, a case can be made for using silicon carbide instead of cordierite to create catalytic monoliths capable of handling a wider variety of inlet flow rates.

The results also show that the ignition and blowout limits vary significantly between split and continuous tubes at high inlet flow speeds when the monolith tube walls are constructed from materials with high thermal conductivity; in this case, silicon carbide. For high inlet flow speeds there are significant differences between split and continuous tubes for the high thermal conductivity material. For monolith tubes constructed from materials with low thermal conductivity, such as the case of cordierite, there are no significant differences between split and continuous tubes over the entire flammability range. Additionally, for high thermal conductivity materials with low inlet flow speeds and low thermal conductivity materials for all inlet flow

speeds over the range of ignition, the fuel conversion percentage does not significantly change and therefore, appears to be independent of inlet flow speed. These results imply that axial heat conduction, or lack thereof due to thermal contact resistance from an air-gap between the end-to-end monolith plugs, through the walls of the monolith results in thermal non-equilibrium between the solid and fluid phase, and subsequently affects ignition and flame stability in catalytic combustion.

ACKNOWLEDGMENTS

I would like to thank my advisor Dr. Sandip Mazumder for the opportunity he granted me to work on this research project and the continued encouragement he provided. None of this could have been accomplished without his guidance and support. This research project has enhanced my entire undergraduate engineering experience. It extended my learning within the academic level and increased my ability to critically analyze issues that arise in practice. Most of all, it has connected me with The Ohio State University on a much deeper level than I ever could have expected, and for this I am extremely grateful.

My appreciation also goes to Dr. Jim Schmiedeler, coordinator of the Mechanical Engineering Honors Program. His development of the overall program furthered the research experience, and his overseeing of the honors research classroom experience allowed students to collaborate on their progress. This research was supported in part by an undergraduate honors fellowship awarded by The Ohio State College of Engineering through the Mechanical Engineering Honors Program.

ESI Group, North America, is acknowledged for providing licenses of *CFD-ACE*+™.

To my parents Howard and Rebecca and my brother John.

You will always be my center, helping remind me of my life's focus.

VITA

Michael Christopher Grimm was born July 3, 1984 at Riverside Methodist Hospital in Columbus, OH. He grew up in Dublin, OH with his parents Howard and Rebecca Grimm and his brother John. In October of 2000, Michael achieved the rank of Eagle Scout in the Boy Scouts of America, earning the Buckeye District Outstanding Eagle Project Award and Presidential Youth Service Award for his completed Eagle project. After graduating from Dublin Scioto High School, Michael moved on to The Ohio State University. While at The Ohio State University, he majored in Mechanical Engineering and minored in English. Through his engineering internships, collegiate coursework, and research efforts, Michael attained a wide breadth of knowledge that furthered the value of his degree and college experience. He is a member of the American Society of Mechanical Engineers, the American Nuclear Society, the American Society of Heating, Refrigerating, and Air-Conditioning Engineering, and TEXNIKOI, an honorary society of The Ohio State University College of Engineering. In November 2006, Michael presented his findings at the Sigma Xi Student Research Conference and received the rating of Excellent. Following graduation, he hopes to apply the knowledge he acquired from these experiences to his employment with General Mills in Hannibal, MO.

TABLE OF CONTENTS

LIST OF FIGURES

LIST OF TABLES

NOMENCLATURE

$\mathbf{B}$	body force vector (m s^{-2})
$c_{p,k}$	specific heat capacity of species k (J kg^{-1} K^{-1})
$\mathcal{D}_{kn}$	binary diffusion coefficient of species k into n (m^2/s)
D_{km} , D_{k}	effective diffusivity of species k into the mixture (m^2/s)
h	enthalpy of mixture (J/kg)
h_k	enthalpy of the k-th species (J/kg)
$h^0_{f,k}$	enthalpy of formation of species k at standard state (J/kg)
$\mathbf{J}_k$	diffusion mass flux of the k-th species
k_c	thermal conductivity of mixture (W m^{-1} K^{-1})
M	molecular weight of the mixture (kg/kmol)
M_k	molecular weight of k-th species (kg/kmol)
$\hat{\mathbf{n}}$	unit surface normal vector
N	total number of species in the mixture
p	pressure (Pa)
$\mathbf{q}$	heat flux (W m^{-2})
$\mathbf{q}_C$	heat flux due to conduction (W m^{-2})
$\mathbf{q}_D$	heat flux due to inter-diffusion of species (W m^{-2})
$\mathbf{q}_R$	heat flux due to radiation (W m^{-2})
Re, Re_D	Reynolds number based on the tube inner diameter
$\dot{R}_k$	production rate of species due to heterogeneous reactions (kmol m^{-2} s^{-1})

$\dot{S}_k$	production rate of k-th species (kg m^{-3} s^{-1})
$\dot{S}_h$	volumetric heat generation rate (W m^{-3})
T	temperature (K)
U	mass averaged velocity (m/s)
X_k	mole fraction of *k*-th species
Y_k	mass fraction of *k*-th species

Greek

Λ_k	molar concentration of species *k* at fluid-solid interface (kmol m^{-3})
μ	dynamic viscosity of mixture (kg m^{-1} s^{-1})
ρ	mixture density (kg m^{-3})
ô	shear stress (N m^{-2})

Chapter 1

INTRODUCTION

1.1 Technology Background

Catalytic converters are used in a wide range of engineering applications, including the fields of automotive exhaust after-treatment, hydrogen production for fuel cell systems, and low temperature lean combustion within gas turbines. Catalytic conversion is utilized in automobiles to remove pollutants from engine exhaust to comply with set governmental emission standards. The two types of converters that have been used are bead-pellet catalytic reactors and catalytic monoliths. Bead/pellet catalytic reactors are constructed by filling a containing vessel with small porous ceramic pellets that have been covered in catalytic slurry (Fig. 1.1 (a)). Catalytic monoliths are a newer technology, though they are made of similar materials as bead/pellet reactors and are constructed of multiple small tubes (Fig. 1.1 (b)). These tubes are made up of a porous ceramic material and covered with a reactive catalyst. Figure 1.2 is a picture of a catalytic converter utilized in exhaust treatment, and clearly shows two catalytic monoliths placed end-to-end inside the converter housing. This is a common practice in industry to achieve the desired conversion percentage. The exhaust flows through the monolith tubes, reacting with the catalyst along the inner surface areas of the tubes and exiting as acceptable emissions.

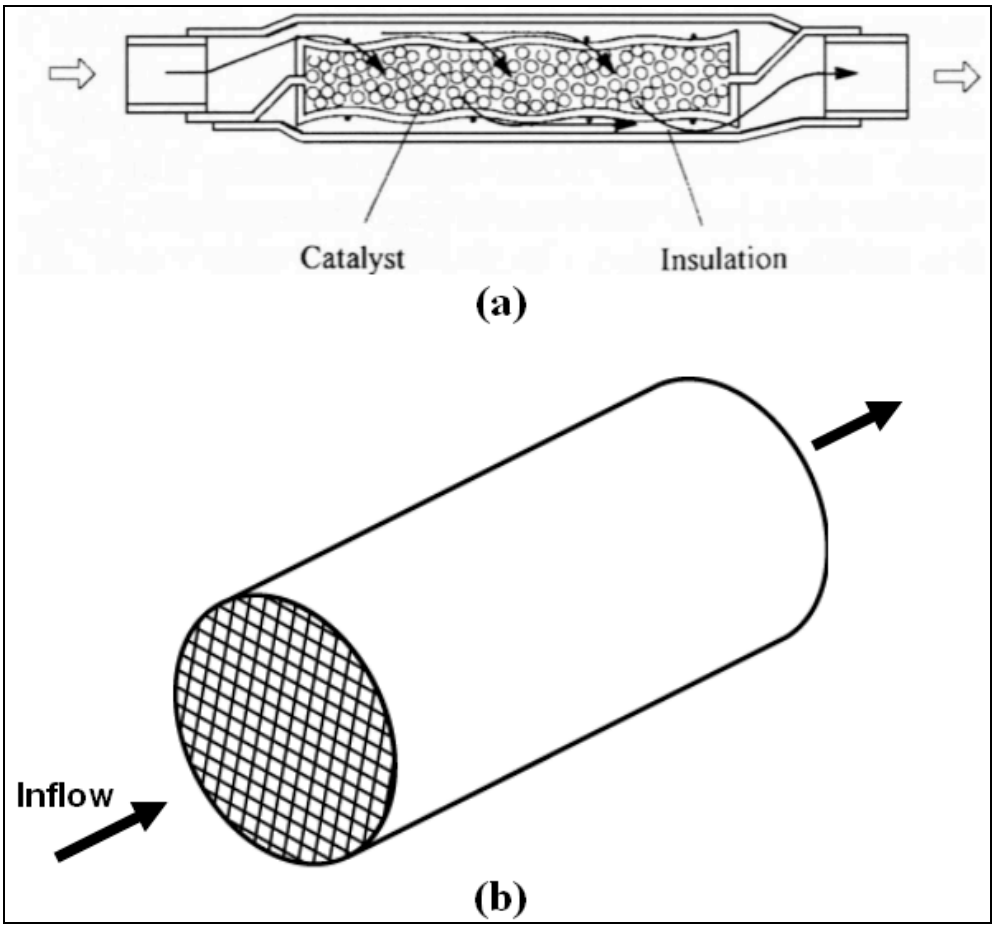

Figure 1.1: Examples of (a) bead/pellet catalytic reactor and (b) catalytic monolith

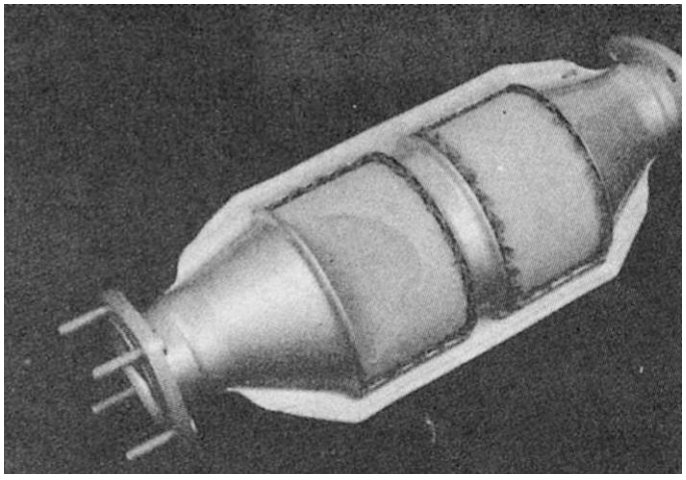

Figure 1.2: Fully assembled automobile catalytic converter with two visible catalytic monoliths

The closed-loop-controlled three-way-catalytic converter is most commonly used catalytic monolith in automotive applications [Ertl (1999)], given its name for the three primary

pollutants it removes. Carbon monoxide (CO), hydrocarbons (HCs), and nitrous oxides (NOx) are removed from the exhaust flow via a catalytic combustion reaction. It utilizes an "electrochemical oxygen sensor" [Ertl (1999) 21] that measures the oxygen content of the exhaust flow and relays a signal to a controller in the engine to change the fuel-to-air ratio and thereby adjust the exhaust composition. By changing the fuel-to-air ratio in the engine, the exhaust composition can be regulated to stay within the range of optimal conversion [Heywood (1988)] (Fig. 1.3).

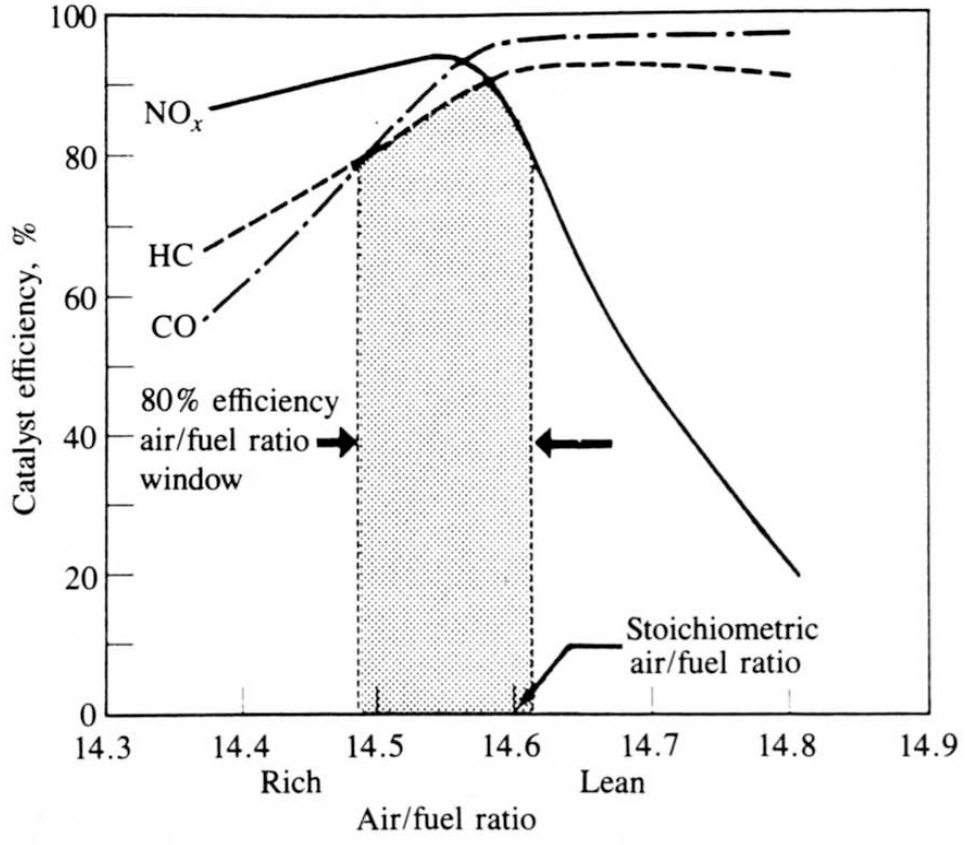

Figure 1.3: Optimal air/fuel ratio range for typical gasoline engine

Catalytic combustors are used in low temperature (typically <1500K) lean combustion within gas turbines to reduce NOx emissions and to allow for greater control of the combustion

process. Adiabatic combustion chambers can lead to high steady-state temperatures capable of damaging the setup, as well as uncontrollable fluctuations known as combustion instabilities that can resonate and bring about destruction within the combustion chamber. The use of catalytic converters for the combustion process results in lower temperatures and an easily controlled laminar flow in and out of the catalytic monolith. Additionally, the use of a catalytic combustor reduces the "nitrogen oxide emissions" while still maintaining the efficiencies typical of gas turbines [N.A.S.A. (1998)]. This is because N_2 and O_2 in air react only above 2000K to produce NOx.

While evidence of CFD modeling of single monolith tubes is abundant in the literature [Deutschmann *et al*. (1994), Hayes and Kolaczkowski (1997), Deutschmann and Schmidt (1998), Raja *et al*. (2000), and the references cited therein], to the best of the authors' knowledge none of the past studies have aimed to address the specific issue at hand, i.e. the effect of thermal conductivity of the monolith support on catalytic combustion of hydrocarbons. Notable amongst related past studies is a recent numerical investigation by Stutz and Poulikakos (2005), which shows that wall heat conduction effects can be non-negligible in monolithic converters for partial oxidation (not combustion) applications. Also, these authors did not attempt to investigate the effect of splitting the monolith tube.

1.2 Motivation for Current Research

Though its range of uses is expansive, the geometry and construction of catalytic monoliths is consistent throughout its disciplines. Catalytic monoliths are composed of many porous ceramic tubes, typically 1mm x 1mm in cross-section, placed into a larger block. The interior of the tubes are then coated with porous catalytic slurry that reacts with the incoming

flow. For automotive exhaust applications, alumina washcoat infused with platinum and rhodium [Heywood (1988)] is used to remove the pollutants, while for hydrocarbon combustion, platinum is used as the catalyst [Deustchmann *et al.* (1994)]. In automotive applications, cordierite is the most common material used due to its low thermal conductivity and thus it was chosen for this study [Lynch (1975), Heywood (1988), Ramesh *et al.* (1997), Riedel (2000)]. To explore results at the opposite end of the spectrum, silicon carbide was chosen because it is another common ceramic used in engineering applications and has a high thermal conductivity. The effect of thermal conductivity is investigated in this project by running simulations similar in all characteristics except the ceramic material composing the catalytic monolith tube walls. By determining the effect of thermal conductivity on the ignition, flame stability, and steady state characteristics of the combustion process, decisions can be made regarding the type of material that is best suited for the design of a monolithic catalytic converter.

Another similarity that pervades through all uses is the view is that an ideal catalytic converter is one that achieves complete conversion of the incoming flow without wasting any catalyst. One of the critical parameters in the design optimization of catalytic converters is the length of the monolith plug to be used. In practice, the length is adjusted to near-optimum by stacking together several monolith plugs end-to-end. Typically, plugs of 1 inch length are used as building blocks. One critical question that arises out of this practice is whether a monolith tube of length $2L$ will exhibit the exact same behavior as two tubes of length L stacked end-to-end (Fig. 1.4). Recent experimental observations for lean NOx trap (LNT) converters [Choi *et al*. (2006)] appear to indicate that the behavior seen in the two scenarios just described may not always be the same. Such experimental data are very limited and require corroboration through further carefully controlled experimental studies. Furthermore, because of the complex nature of

operation of LNT converters, it is not clear if any discrepancies are due to the splitting of the monolith tube or other unforeseen experimental errors. Nevertheless, from a theoretical standpoint, it is credible to accept that a difference may exist. One of the possible reasons for differences in the behavior between continuous and split monoliths is different axial heat conduction through the walls of the monolith.

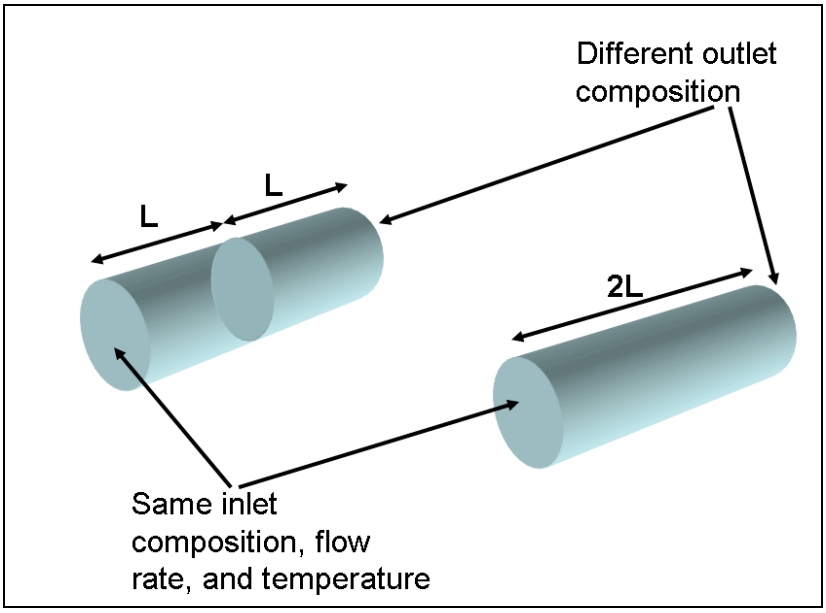

Figure 1.4: Schematic representation of split and continuous monolith tubes demonstrating the problem under consideration in this study

1.3 Objectives

The broad objectives of the present study are to elucidate behavioral differences in ignition and steady state combustion characteristics due to differences in the material comprising the catalytic monolith tube and to determine the effects of using split and continuous catalytic monolith tubes through computational fluid dynamic (CFD) simulations. The specific objectives are as follows:

- Investigate the effect of thermal conductivity of the ceramic support material used for the catalytic monolith on the combustion of a hydrocarbon fuel, namely methane.
- Investigate the effect of split and continuous catalytic monolith tubes on ignition, flame stability, and steady state combustion of a gaseous hydrocarbon fuel.

1.4 Organization of this Thesis

This thesis is divided into multiple sections, beginning with an introduction to catalytic combustion material and a discussion of the motivation behind and objectives of this research in Chapter 1 (Introduction). Next, there is a description of methods undertaken in this research in Chapter 2 (Research Method), including the governing equations that were solved using the commercial software *CFD-ACE+*™ as well as the strategy employed in arriving at the previously listed objectives. There is a discussion of the results obtained from the solved computer simulations with regards to the effects of thermal conductivity of the ceramic comprising the catalytic monolith channel and the effect of splitting the catalytic monolith tube in Chapter 3 (Results and Discussion). Finally, the implications of the research results are discussed in Chapter 4 (Summary and Conclusions) and extended in Chapter 5 (Future Work).

Chapter 2

RESEARCH METHOD

2.1 Governing Equations

The governing equations are the equations of conservation of mass (both overall and individual species), momentum and energy, and are written as [Kuo (1986), Bird *et al*. (2001)]:

Overall mass: $\frac{\partial}{\partial t}(\rho) + \nabla \circ (\rho \mathbf{U}) = 0$ (1)

Momentum: $\frac{\partial}{\partial t}(\rho \mathbf{U}) + \nabla \circ (\rho \mathbf{U}\mathbf{U}) = -\nabla p + \nabla \circ \hat{\mathbf{o}} + \rho \mathbf{B}$ (2)

Energy: $\frac{\partial}{\partial t}(\rho h) + \nabla \circ (\rho \mathbf{U} h) = -\nabla \circ \mathbf{q} + \dot{S}_h$ (3)

Species mass: $\frac{\partial}{\partial t}(\rho Y_k) + \nabla \circ (\rho \mathbf{U} Y_k) = -\nabla \circ \mathbf{J}_k + \dot{S}_k \qquad \forall k = 1,2,\ldots,N$ (4)

where ρ is the mixture density, p is the pressure, $\hat{\mathbf{o}}$ is the shear stress tensor, and $\mathbf{B}$ is the body force vector. Equations (1) and (2) are the well known Navier-Stokes equations, and need no further discussion. In Eq. (4), Y_k is the mass fraction of the *k*-th species, $\mathbf{J}_k$ is the mass diffusion flux of the *k*-th species, and $\dot{S}_k$ is the production rate of the *k*-th species due to homogeneous chemical reactions. The total number of gas-phase species in the system is denoted by *N*. In Eq. (3), $\dot{S}_h$ represents the net source due to viscous dissipation and other work and heat interactions, and $\mathbf{q}$ denotes the net heat flux due to molecular conduction, radiation, and inter-species diffusion, and is written as [Bird *et al*. (2001)]:

$$\mathbf{q} = \mathbf{q}_C + \mathbf{q}_R + \mathbf{q}_D = -k_c \nabla T + \mathbf{q}_R + \sum_{k=1}^{N} \mathbf{J}_k h_k \quad (5)$$

where h_k is the enthalpy of the *k*-th species, k_c is the thermal conductivity of the mixture, and h is the enthalpy of the mixture (= $\sum_{k=1}^{N} h_k Y_k$). The heat flux due to inter-diffusion of species, $\mathbf{q}_D$, is often neglected in reacting flow formulations without any justification. In many practical applications of multi-species flows, this term can be comparable or larger than the Fourier conduction flux $\mathbf{q}_C$, and can result in net heat flux that is opposite in direction to the imposed temperature gradient [Kumar and Mazumder (2006)]. In the above formulation, the enthalpy of the *k*-th species, h_k , includes the enthalpy of formation and the sensible enthalpy, and is written as

$$h_k(T) = h_{f,k}^0 + \int_{T_0}^{T} c_{p,k}(T)dT \qquad (6)$$

where $h_{f,k}^0$ is the enthalpy of formation of species *k* at the standard state, and $c_{p,k}$ is the specific heat capacity of species *k*. The species enthalpy is generally computed using standard thermodynamic databases, such as the JANNAF database.

The diffusion flux in a multi-component system is often modeled using the so-called dilute approximation [Bird et al. (2001), Sutton and Knoffo (1998), Wangard *et al*. (2001), Desilets *et al*. (1997)]. In a recent study [Kumar and Mazumder (2007)], it has been shown that for catalytic combustion applications, the dilute approximation is comparable in accuracy to a rigorous multi-component diffusion formulation derived from the Stefan-Maxwell equations, while being computationally about twice as efficient. Thus, the dilute approximation is used here. Using the dilute approximation, the diffusion flux is written as [Bird *et al.* (2001), Sutton and Knoffo (1998), Wangard *et al*. (2001), Desilets *et al*. (1997)]

$$\mathbf{J}_k = -\rho \mathsf{D}_{km} \nabla Y_k \qquad (7)$$

where D_{km} is the effective diffusivity of species *k* into the mixture, and is henceforth denoted by D_k for simplicity. The effective diffusivity is given by the relation [Bird *et al.* (2001)]

$$\mathsf{D}_{km} = \mathsf{D}_k = (1 - X_k) / \sum_{\substack{i=1 \\ i \neq k}}^{N} \frac{X_i}{\mathcal{D}_{ki}} \tag{8}$$

Substitution of Eq. (7) into Eq. (4) yields the appropriate species transport equation for the dilute approximation formulation:

$$\frac{\partial}{\partial t}(\rho Y_k) + \nabla \circ (\rho \mathbf{U} Y_k) = \nabla \circ \left(\rho \mathsf{D}_k \nabla Y_k\right) + \dot{S}_k \qquad \forall k = 1,2,\ldots,N \tag{9}$$

Radiation is the dominant mode of heat transfer in such high-temperature applications. In a separate related study [Mazumder and Grimm (2007)], detailed participating medium radiation calculations using Planck mean absorption coefficients of the gas mixture were performed, and it was found that the combustion gas within the monolith tube hardly affects the radiation field, since these tubes are narrow (2 mm outer diameter). The optical thickness of the gas channels is, therefore, very small, and the gas can be considered non-participating. Thus, for the present study, only radiation exchange between surfaces was considered. Such an approximation has also been used by past researchers [Boehman (1998)] for modeling radiative transport in monolith tubes. In the present study, the discrete ordinates method with the S_4 approximation was used to solve the radiative transport equation. The relevant discrete ordinates equations are readily available from the text by Modest (2003), and are omitted here for the sake of brevity.

The governing equations, just described, require boundary conditions. The boundary conditions for the mass and momentum conservation equations are the no-slip conditions at walls, and appropriate mass flux or pressure boundary conditions at inflow and outflow boundaries. These boundary conditions and their numerical implementation are well known and

need no further discussion. The focus of this discussion is the boundary conditions for species and energy associated with heterogeneous chemical reactions at fluid-solid interfaces.

At a reacting surface, the diffusion flux of species is balanced by the reaction flux since the surface cannot store any mass. At the heart of surface reaction processes is adsorption and desorption of species at the surface, the treatment of which requires inclusion of so-called surface-adsorbed species [Coltrin *et al*. (1991)]. At steady state, the net production rate of the surface-adsorbed species is zero. In the absence of etching or deposition of material from the surface (*i.e*., zero Stefan flux), the reaction-diffusion balance equation at the surface may be written as [Coltrin *et al*. (1991), Mazumder and Lowry (2001)]

$$\mathbf{J}_k \circ \hat{\mathbf{n}} = M_k \dot{R}_k \qquad \forall k \in \text{gas - phase species} \tag{10a}$$

$$\dot{R}_k = \begin{cases} d\Lambda_k / dt & \text{for unsteady} \\ 0 & \text{for steady} \end{cases} \qquad \forall k \in \text{surface - adsorbed species} \tag{10b}$$

where $\dot{R}_k$ is the molar production rate of species *k* due to heterogeneous chemical reactions, Λ_k is the molar concentration of species *k* at the fluid-solid interface, and $\hat{\mathbf{n}}$ is the outward unit surface normal. Since $\dot{R}_k$ is an extremely nonlinear function of the molar concentrations (or mass fractions) [Coltrin *et al*. (1991), Mazumder and Lowry (2001)], Eq. (10) represents a nonlinear set of differential algebraic equations (DAE). The solution of this stiff set of nonlinear DAE is generally obtained using the Newton method, but requires special pre-conditioning to address stiffness and ill-posed-ness in the case of steady state solutions. Details pertaining to these numerical issues may be found elsewhere [Mazumder and Lowry (2001)]. The solution of Eq. (10) provides the near-wall mass fractions and mass fluxes [represented by the left hand side of Eq. (10b)] of all gas-phase species, which appear as sources/sinks for control volumes adjacent to the surface in a finite-volume formulation [Mazumder and Lowry (2001)].

The balance of energy at the surface yields the following equation

$$\left[-k\nabla T + \mathbf{q}_R + \sum_{k=1}^{N} \mathbf{J}_k h_k \right]_F \circ \hat{\mathbf{n}} = \left[-k\nabla T + \mathbf{q}_R \right]_S \circ \hat{\mathbf{n}} \qquad (11)$$

where the subscript "*F*" denotes quantities on the fluid side of the fluid-solid interface, while the subscript "*S*" denotes quantities on the solid side of the same interface. The solution of Eq. (11), which is also a nonlinear equation, yields the temperature at the fluid-solid interface, and subsequently provides the flux of energy at the interface, which can then be used as a source/sink for the cells adjacent to the interface after appropriate linearization. In this enthalpy formulation, the heat of surface reaction actually manifests itself through the $\sum \mathbf{J}_k h_k$ term—another reason why the energy carried by species inter-diffusion should never be neglected for such applications.

Equations (1), (2), (3) along with Eq. (9), when solved along with the appropriate boundary conditions described, will produce flow, temperature and mass fraction distributions of all species within the monolith tube. These equations were solved using the commercial CFD code, *CFD-ACE+*™, and the procedure that was employed to do so is discussed next.

2.2 Solution Strategy

Modeling the catalytic converter tube was conducted in three major steps: geometric modeling and mesh generation, model setup, and post-processing. A geometry file and mesh were created using the program *CFD-GEOM* (Fig. 2.1 (a)). The geometry that was created and meshed is representative of a single tube at the very center of the catalytic monolith (Fig. 2.2). The geometry was modeled as a cylinder of outer diameter *D*, a wall thickness of 0.1*D*, and a length of 2*L*. Figure 2.2 shows a schematic of the model that was used. It is customary to treat

individual channels within a monolithic catalytic converter as channels of circular cross-section [Deutschmann and Schmidt (1998), Raja *et al*. (2000), Stutz and Poulikakos (2005)] because they form this shape when the alumina catalyst forms on the square ceramic channel walls (Fig. 2.2). Since the tube is cylindrical, azimuthal symmetry is assumed, and the computer model was designed to be axisymmetric rather than full 3D. This was done to increase the speed of simulation completion. The geometric program was also used to develop a mesh grid capable of sufficiently resolving the physics at all length scales. All simulations were performed on a uniform grid with 150 cells in the axial direction and 48 cells in the radial direction. A grid independence study for nominal parameter values showed that calculations on a 300 x 96 grid yield results that are within 1% of the values from the 150 x 48 grid, and thus the coarser of the two meshes was used for further parametric studies and accepted as accurate.

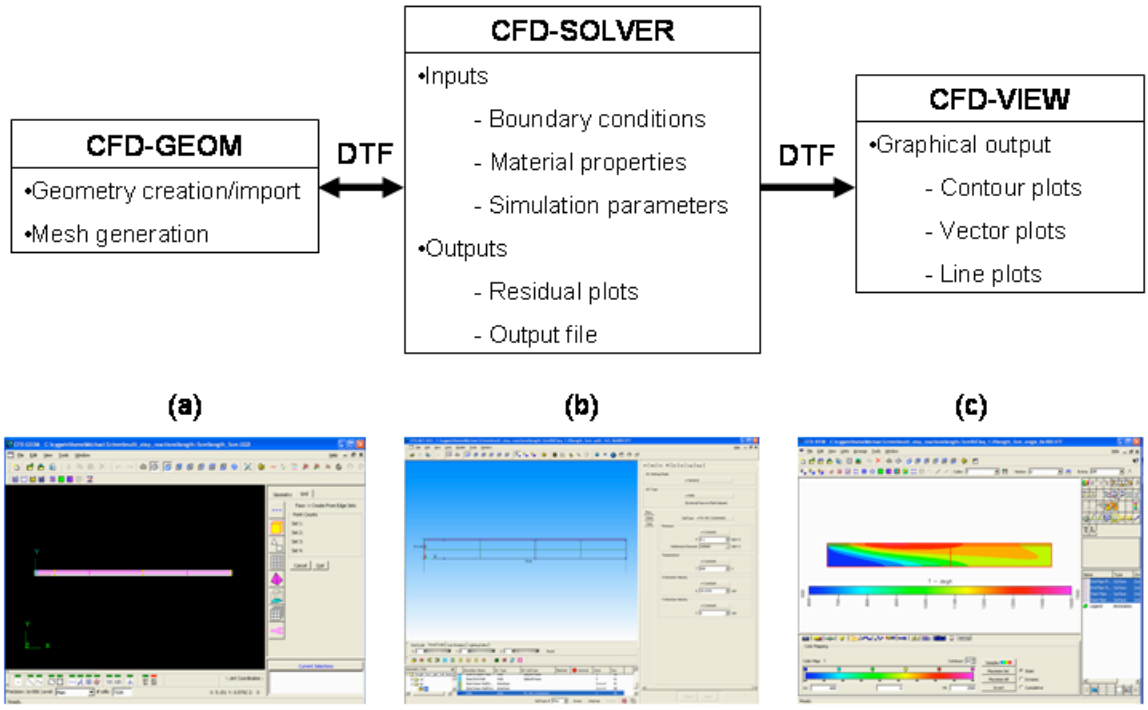

Figure 2.1: Snapshots of CFD- (a) GEOM, (b) SOLVER, and(c) VIEW illustrating the working mechanism of the commercial software CFD-ACE+^{TM}

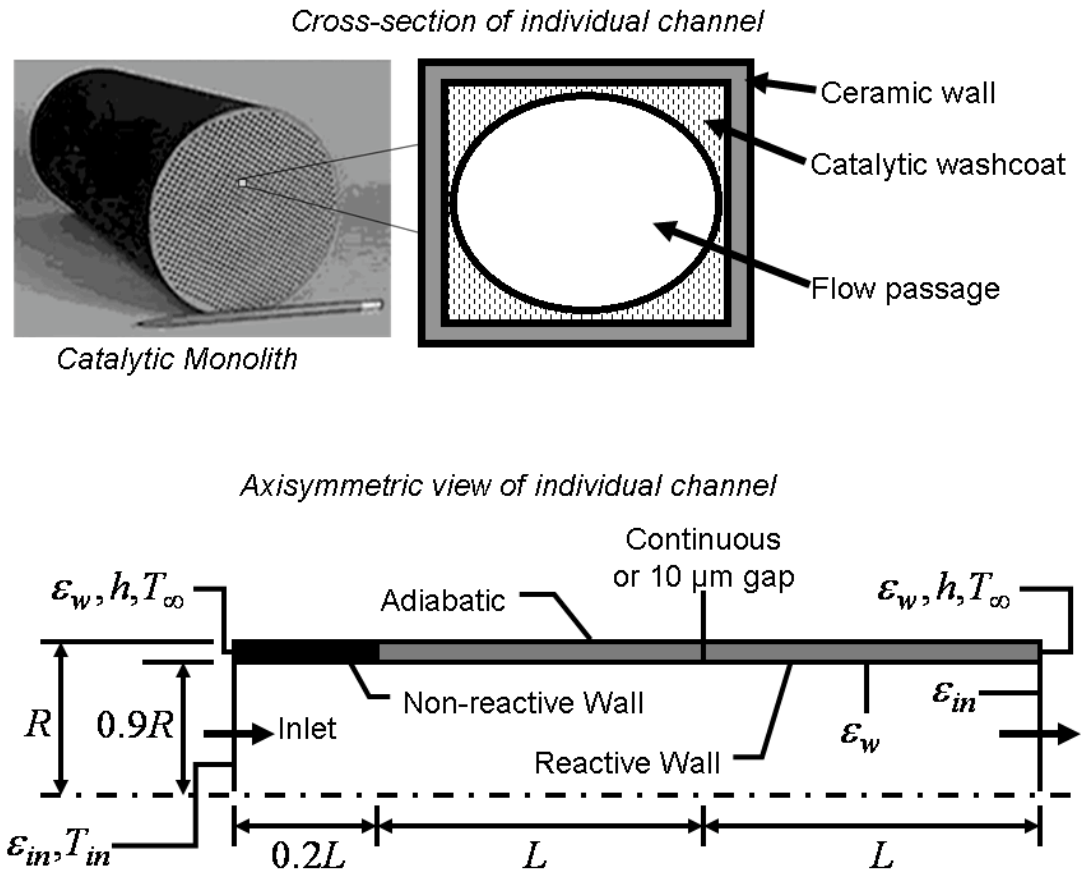

Figure 2.2: Illustration of a full-scale catalytic converter and the reduced axisymmetric model of one of its individual channels used for numerical simulations in this study

The faces of the cross-section were set, grid points were added to each face side, and from these points an appropriate grid was generated, as shown in Figure 2.1 (a). This mesh file was saved and then the data was transferred into another program called *CFD-SOLVER* (Fig. 2.1 (b)) via a binary, so-called DTF file. The purpose of this program is to set up the boundary conditions and material properties for the simulation at hand. These material properties include the density, thermal conductivity, emissivity, etc., of all regions/materials. The boundary conditions were set for temperature, emissivity, equivalence ratio of the inlet, emissivity and equivalence ratio of the outlet, the reactive and inactive section of the inner wall, and the exterior

ambient conditions, among others. Once the simulation was correctly setup, it was run through the built-in solver (which solves the equations described in Section 2.1) to determine the steady state or transient solution. The solver employs an iterative technique to attain convergence. The residuals of each of the governing equations are tracked as they progress towards the desired convergence level (Fig. 2.3). Finally, distributions of all relevant quantities such as flow velocity, temperature, pressure, etc., are printed out in the same DTF file. This file can be then be opened using *CFD-VIEW* (Fig. 2.1 (c)) in order to graphically view and analyze the data. In addition, *CFD-SOLVER* prints an ASCII output file with relevant processed data (Fig. 2.4).

Figure 2.3: Visual plot of residuals for each governing conservation equation

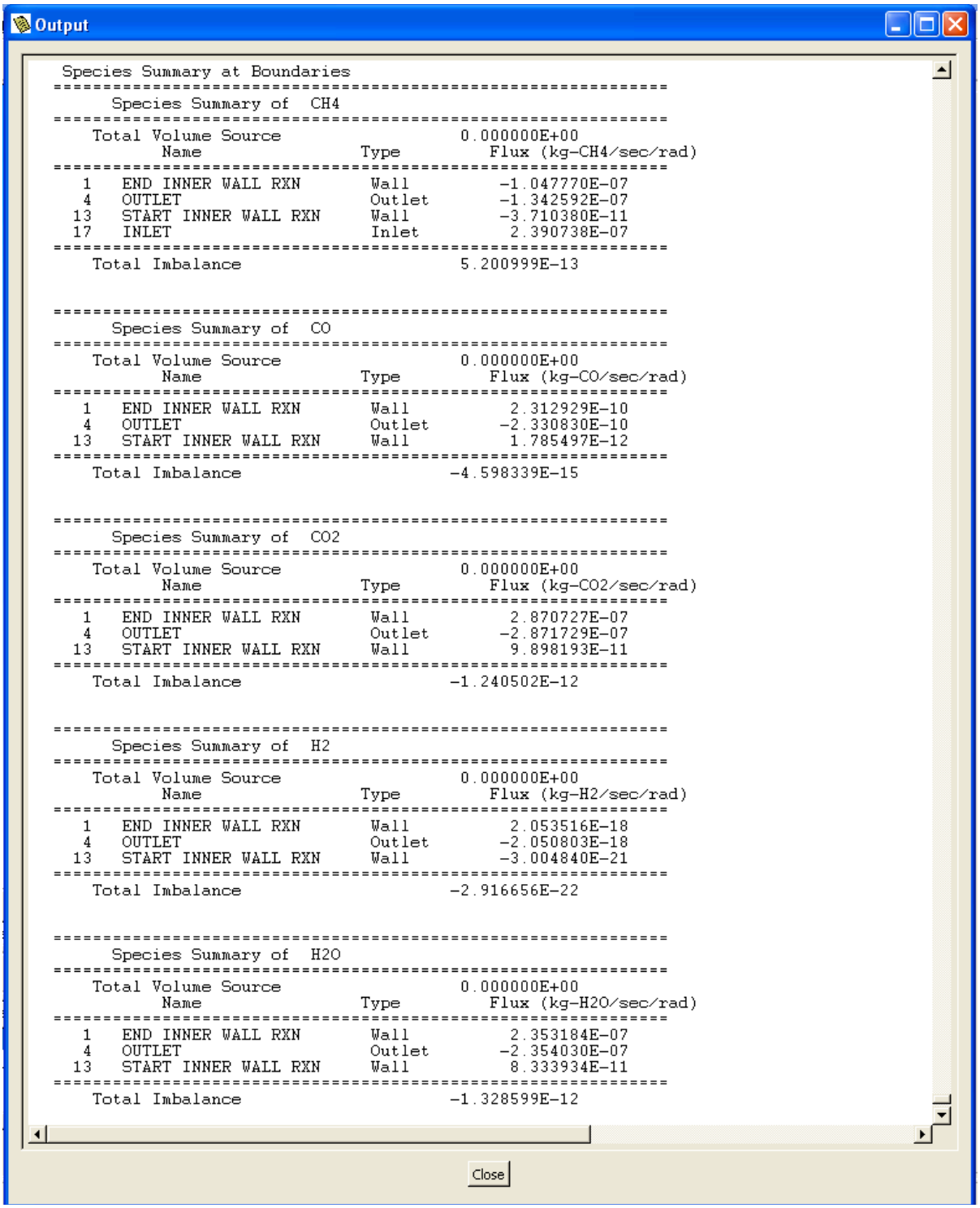

Figure 2.4: Numerical output file generated by CFD-SOLVER

Chapter 3

RESULTS AND DISCUSSION

3.1 Cases Studied

For the present study, catalytic combustion of methane on platinum is chosen as the candidate system because the kinetics of methane combustion on platinum are reasonably well known [Deutschmann *et al*. (1994), Raja *et al*. (2000)], and also because catalytic combustion of hydrocarbons constitutes an important class of applications as previously described. Furthermore, the particular reaction mechanism that has been used here has been validated extensively [Deutschmann *et al.* (1994), Raja *et al*. (2000), Mazumder and Sengupta (2002)]. Table 1 shows the full reaction mechanism. It is comprised of 24 surface reactions between 19 species. Table 2 summarizes the parameters used for the simulations. To enable study of wall heat conduction effects, the two commonly used ceramic materials of silicon carbide, which has a high thermal conductivity, and cordierite, which has a low thermal conductivity, were chosen. Both steady state and transient simulations are performed for both wall materials for various flow rates (Reynolds numbers) and fuel-air mixtures (equivalence ratios). A methane-air mixture of specified composition was introduced into the monolith tube at a prescribed velocity, and a plug velocity profile was imposed at the inlet. Variation of the inlet velocity translates to a variation in the inlet Reynolds number, $\mathrm{Re}_D = \rho U_{in} D / \mu$, which is one of the parameters in the simulations. The simulations are performed using the commercial CFD code *CFD-ACE+*™, and include fluid flow, heat transfer by all three modes, multi-component species transport, and multi-step finite-rate heterogeneous chemistry. Predicted results for species mass fraction distributions, temperature distributions, and conversion percentages are carefully analyzed to

gain insight into the ignition, blowout, and steady state combustion phenomena in such systems, with particular emphasis on the differences between split and continuous tubes.

Table 1: Reaction mechanism for methane combustion on a Platinum surface

	Reaction	A^a	β^a	E^a
(1)	$H_2 + 2Pt(s) \rightarrow 2H(s)$	4.46×10^{10}	0.5	
	The reaction rate is first-order in Pt(s)			
	The reaction has an equivalent sticking coefficient of 0.046			
(2)	$2H(s) \rightarrow H_2 + 2Pt(s)$	3.7×10^{21}		67.4
	The reaction rate is modified by an activated H(s) coverage,[b] i.e., $k = AT^{\beta}\exp(-E/RT) \times \exp(-\epsilon[H(s)]/RT)$, where the activation parameter $\epsilon = -6$ kJ/mol			
(3)	$H + Pt(s) \rightarrow H(s)$	1.00[c]		
(4)	$O_2 + 2Pt(s) \rightarrow 2O(s)$	1.8×10^{21}	−0.5	
(5)	$O_2 + 2Pt(s) \rightarrow 2O(s)$	0.023[c]		
	Reactions (4) and (5) represent alternative competing pathways			
(6)	$2O(s) \rightarrow O_2 + 2Pt(s)$	1.8×10^{21}		213.2
	The reaction rate is modified by an activated O(s) coverage			
	The activation parameter $\epsilon = -60$ kJ/mol			
(7)	$O + Pt(s) \rightarrow O(s)$	1.0[c]		
(8)	$H_2O + Pt(s) \rightarrow H_2O(s)$	1.0[c]		
(9)	$H_2O(s) \rightarrow H_2O + Pt(s)$	1.0×10^{13}		40.3
(10)	$OH + Pt(s) \rightarrow OH(s)$	1.0[c]		
(11)	$OH(s) \rightarrow OH + Pt(s)$	1.0×10^{13}		192.8
(12)	$H(s) + O(s) \leftrightarrow OH(s) + Pt(s)$	3.7×10^{21}		11.5
(13)	$H(s) + OH(s) \leftrightarrow H_2O(s) + Pt(s)$	3.7×10^{21}		17.4
(14)	$OH(s) + OH(s) \leftrightarrow H_2O(s) + O(s)$	3.7×10^{21}		48.2
(15)	$CO + Pt(s) \rightarrow CO(s)$	1.618×10^{20}	0.5	
	The reaction rate is second order in Pt(s)			
	The reaction is equivalent to a sticking coefficient of 0.84			
(16)	$CO(s) \rightarrow CO + Pt(s)$	1.0×10^{13}		125.5
(17)	$CO_2(s) \rightarrow CO_2 + Pt(s)$	1.0×10^{13}		20.5
(18)	$CO(s) + O(s) \rightarrow CO_2(s) + Pt(s)$	3.7×10^{21}		105.0
(19)	$CH_4 + 2Pt(s) \rightarrow CH_3(s) + H(s)$	4.63×10^{20}	0.5	
	The reaction rate has a 2.3 order dependence on Pt(s)			
	The reaction is equivalent to a sticking coefficient of 0.01			
(20)	$CH_3(s) + Pt(s) \rightarrow CH_2(s)s + H(s)$	3.7×10^{21}		20.0
(21)	$CH_2(s)s + Pt(s) \rightarrow CH(s) + H(s)$	3.7×10^{21}		20.0
(22)	$CH(s) + Pt(s) \rightarrow C(s) + H(s)$	3.7×10^{21}		20.0
(23)	$C(s) + O(s) \rightarrow CO(s) + Pt(s)$	3.7×10^{21}		62.8
(24)	$CO(s) + Pt(s) \rightarrow C(s) + O(s)$	1.0×10^{18}		184.0

[a] Arrhenius parameters for the rate constants written in the form: $k = AT^{\beta}\exp(-E/RT)$. The units of A are given in terms of moles, cubic meters, and seconds. E is in kJ/mol.

[b] The surface coverage (e.g., $[H(s)]$) is specified as a site fraction.

[c] Sticking coefficient. Total available site density for Pt is $\Gamma = 2.7 \times 10^{-9}$ mol/cm^2.

Table 2: Values of various parameters used for numerical simulations

Parameter	Value/ Equation/ Description	Comment/ Source
Length of building block, L	2.5 cm	typical value
Outer diameter of tube, D	2.0 mm	typical value
Thickness of tube wall	0.1 mm	typical value
Outer radius of tube, R	1 mm	typical value
Emissivity of wall, ε_w	0.5	assumed
Emissivity of inlet, ε_{in}	1.0	assumed
Convective heat transfer coefficient, h	200 W m^{-2} K^{-1}	assumed
Far field temperature, T_∞	600 K	assumed
Inlet temperature, T_{in}	600 K	typical value
Inlet axial velocity, U_{in}	Obtained from prescribed Re, using $U_{in} = \mathrm{Re}\mu_{in}/(\rho_{in}D)$	
Initial temperature for transient simulations	1000 K everywhere	typically used
Initial composition for transient simulations	Air everywhere	typically used
Fuel equivalence ratio, stoichiometric	1.0	
Fuel equivalence ratio, lean	0.8	assumed
Cordierite Properties		
Thermal conductivity	3 W m^{-1} K^{-1}	Value can vary between 2 and 5 [Lynch (1975)]. Stutz and Poulikakos (2005) used 2.7. Here, 3 is used as a representative value
Density	2511 kg m^{-3}	[Lynch (1975)]
Specific heat capacity	1046 J kg^{-1} K^{-1}	[Lynch (1975)]
Silicon Carbide Properties		
Thermal conductivity	$170.39 - 0.0696T$ W m^{-1} K^{-1}	[Riedel (2000)]
Density	3200 kg m^{-3}	[Riedel (2000)]
Specific heat capacity	$490.52 + 0.6122T$ J kg^{-1} K^{-1}	[Riedel (2000)]

Newton cooling boundary conditions were employed at the ends (both front and back) of the ceramic tubes. As stated earlier, surface-to-surface gray radiation transport was included. The emissivity of the inner walls of the tube was assumed to be 0.5, due to lack of better information. The inlet and the outlet were assumed to have an emissivity of unity, implying that no radiation gets reflected back from these boundaries. Conversion of the fuel is assumed to take place because of heterogeneous (surface) reactions at the walls only. This is justified since the range of temperature observed is such that homogeneous combustion may be neglected [Raja *et al*. (2000)]. All transport properties of the fluid, namely viscosity, thermal conductivity, and binary diffusion coefficients were computed using the Chapman-Enskog equations of kinetic theory [Bird *et al.* (2001), Hirschfelder *et al.* (1954)], available as part of the *CFD-ACE*+™ code. The Lennard-Jones potentials, which are needed as inputs, were obtained from the CHEMKIN database, which is built into the *CFD-ACE*+™ code. The solutions were deemed to be converged when the residuals of each of the conservation equations decreased by five orders of magnitude.

Since the tube at the center of the catalytic monolith was considered for simulation, the wall boundary conditions were set as adiabatic because at the center of the monolith the tube walls immediately adjacent to the center would be undergoing the same processes and therefore have very nearly the same exterior temperature. This would allow very little, if any, heat to exit through the tube walls, and thereby theoretically justifies modeling them as adiabatic. The chemical compositions of the inlet methane-air mixtures were calculated from prescribed equivalence (or fuel-air) ratio values. The following cases were simulated for both silicon carbide and cordierite monolith tubes:

1. *2L* = 1 cm tube
    a. Single step chemistry
        i. Continuous
            1. $\Phi = 1.0$
            2. $\Phi = 0.8$
            3. Transient simulations
        ii. Split (10 μm air gap)
            1. $\Phi = 1.0$
            2. $\Phi = 0.8$
            3. Transient simulations
    b. Multi-step chemistry
        i. Continuous
            1. $\Phi = 1.0$
            2. $\Phi = 0.8$
            3. Transient simulations
        ii. Split (10 μm air gap)
            1. $\Phi = 1.0$
            2. $\Phi = 0.8$
            3. Transient simulations
2. *2L* = 5 cm tube
    a. Single step chemistry
        i. Continuous
            1. $\Phi = 1.0$
            2. $\Phi = 0.8$
            3. Transient simulations
        ii. Split (10 μm air gap)
            1. $\Phi = 1.0$
            2. $\Phi = 0.8$
            3. Transient simulations
    b. Multi-step chemistry
        i. Continuous
            1. $\Phi = 1.0$
            2. $\Phi = 0.8$
            3. Transient simulations
        ii. Split (10 μm air gap)
            1. $\Phi = 1.0$
            2. $\Phi = 0.8$
            3. Transient simulations

The simulations were run to steady state for each case to determine the inlet flow rates where ignition and blowout occurs, and then transient simulations were run to confirm these findings.

The model was built progressively, starting from simple flow and heat transfer calculations to onethat included all relevant physical phenomena. The length 2*L* initially used for simulation was 1 cm, and the preliminary solver runs were done with simple fluid flow without any surface reactions. As the project progressed and the simple flow simulations demonstrated the correct characteristics, the model was extended to include a single step chemical reaction of methane and oxygen on platinum [Song, X., *et al*. (1991)]:

$$CH_4 + 2\ O_2 \rightarrow CO_2 + 2\ H_2O,\ \frac{d[CH_4]}{dt} = -1.3 \times 10^{11} \exp\left(\frac{-16189}{T}\right)[CH_4][O_2]^{1/2} \quad (12)$$

where $[CH_4]$ and $[O_2]$ are the molar concentrations of methane and oxygen, respectively, and T is the surface temperature in Kelvin. $\frac{d[CH_4]}{dt}$ is the molar production rate of methane in kmol/m^3/s. Results were analyzed for the 1 cm tube cases over the relevant range of Reynolds numbers, showing correct trends for the simple combustion reaction but with no significant differences between the continuous and split tube cases as demonstrated through their methane distribution profiles (Fig. 3.1). The cordierite tube simulations of 1 cm length were then tested with multi-step chemical reactions but again there were few differences apparent between the continuous and split tube cases (Fig. 3.2). It is worth noting that ignition phenomena can only be correctly predicted with multi-step finite-rate chemistry, corresponding to two 2-inch building blocks. The catalytic tube model length 2*L* was changed to 5 cm and the multi-step reaction mechanism [Deutschmann *et al*. (1994), Raja *et al*. (2000)], shown in Table 1, was finally used in lieu of simple one-step mechanism. The fuel mixtures that were tested were stoichiometric ($\Phi = 1$), lean 0.9 ($\Phi = 0.9$), and lean 0.8 ($\Phi = 0.8$) equivalence ratios. At first, rich fuel mixtures were also tested but were later abandoned because it is highly uncommon for catalytic combustion processes to be run at rich fuel equivalence ratios.

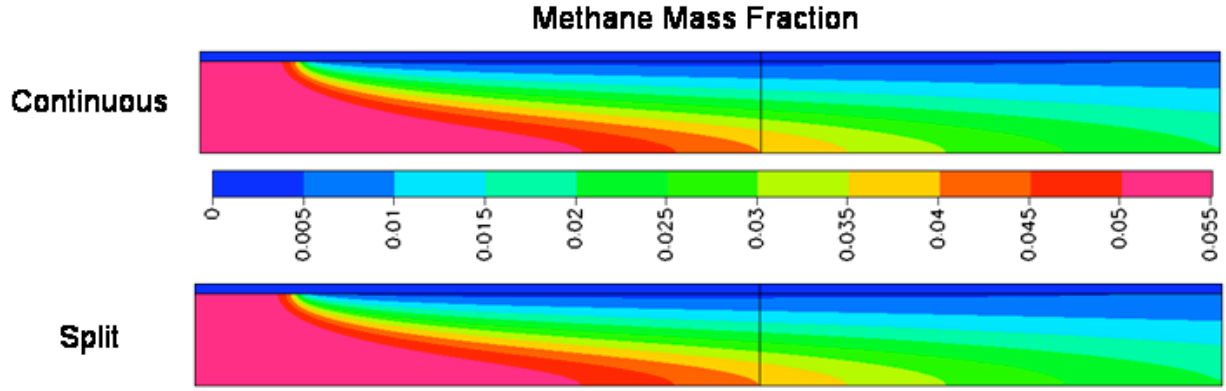

Figure 3.1: Catalytic combustion of a stoichiometric (Φ = 1.0) methane-air mixture on platinum supported on a cordierite monolith at steady state. Re = 100, length 2L=1 cm using a single-step reaction mechanism

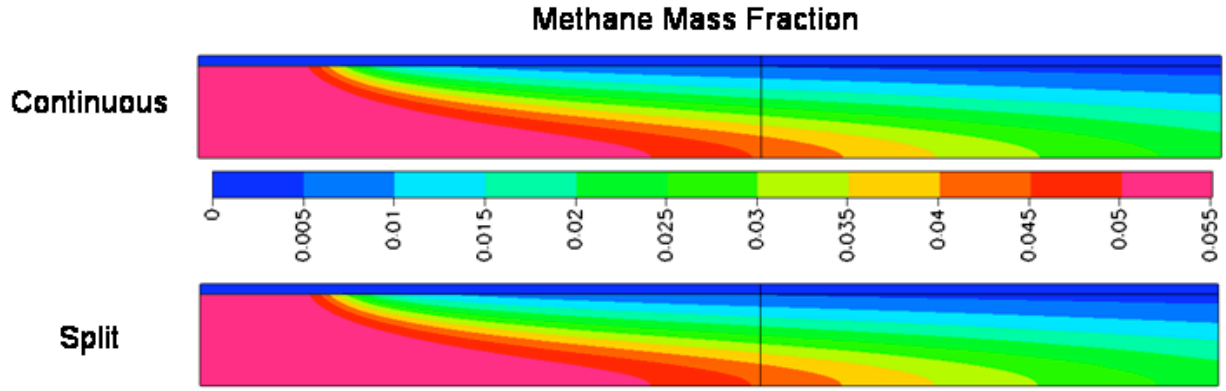

Figure 3.2: Catalytic combustion of a stoichiometric (Φ = 1.0) methane-air mixture on platinum supported on a cordierite monolith at steady state. Re = 100, length 2L=1 cm using a multi-step reaction mechanism

It was initially decided to treat the gap size between two building blocks as a parameter as well. However, it was found that a gap size of 1 μm did not produce any noticeable differences in results between the split and continuous tube. A gap size of 100 μm (0.1 mm) is unrealistic since 0.1 mm is the thickness of the wall of the tube itself. Thus, simulations were

finally performed only with a gap size of 10 μm. Again, the choice was prompted by lack of better information and the fact that the objective of this study is to elucidate behavioral differences, and not necessarily achieve quantitative validation. The mean free path of air at room temperature and pressure is approximately 54 nm, based on kinetic theory calculations [Bird *et al.* (2001)] – about two orders smaller than the gap size used here. Thus, no special thermal contact model was necessary to treat thermal transport within the gap. A simple conductive resistance model was used.

3.2 Effect of Thermal Conductivity

A wide range of inlet flow rates (Reynolds numbers) were simulated for both cordierite and silicon carbide tubes until the full range of stable combustion was determined for both with inlet fuel flows of stoichiometric ($\Phi = 1.0$) and a lean equivalence ratio of $\Phi = 0.8$. The simulations run with a stoichiometric fuel equivalence ratio yielded stable flames, while the simulations completed using a lean 0.8 equivalence ratio did not produce a stable flame at steady-state. It was thought that the lean 0.8 simulations were not producing stable combustion due to the inlet flow temperature being too low at 600K, but even when the inlet flow temperature was raised to 800K, stable combustion was still not achieved.

The range of Reynolds numbers for which ignition occurs in the two cases (silicon carbide *vs.* cordierite) is completely different (Fig. 3.3, 3.5). The ignition occurs over a much wider range in the case of silicon carbide, indicating that it is a better candidate for the development of robust monolith plugs of various lengths. The average thermal conductivity of silicon carbide is approximately 100 W m^{-1} K^{-1}, while that of cordierite is approximately 3 W m^{-1} K^{-1}, so axial heat conduction through silicon carbide is much more pronounced than in cordierite,

enabling heat generated at the point of attachment of the flame to propagate to other locations of the silicon carbide tube, such as the 10 μm air gap, and thereby facilitating the stability of the flame.

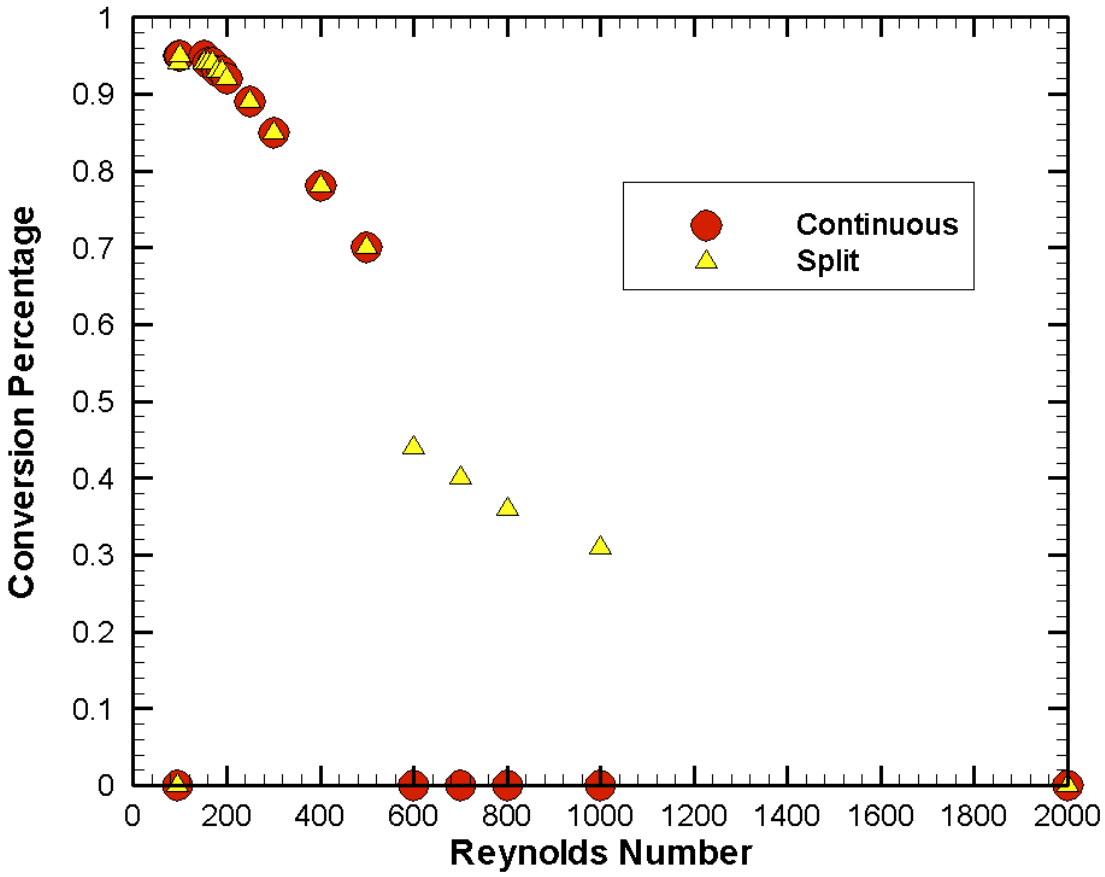

Figure 3.3: Ignition characteristics for heterogeneous combustion of a stoichiometric (Φ = 1.0) methane-air mixture on platinum supported on a silicon carbide monolith with length 2L=5cm

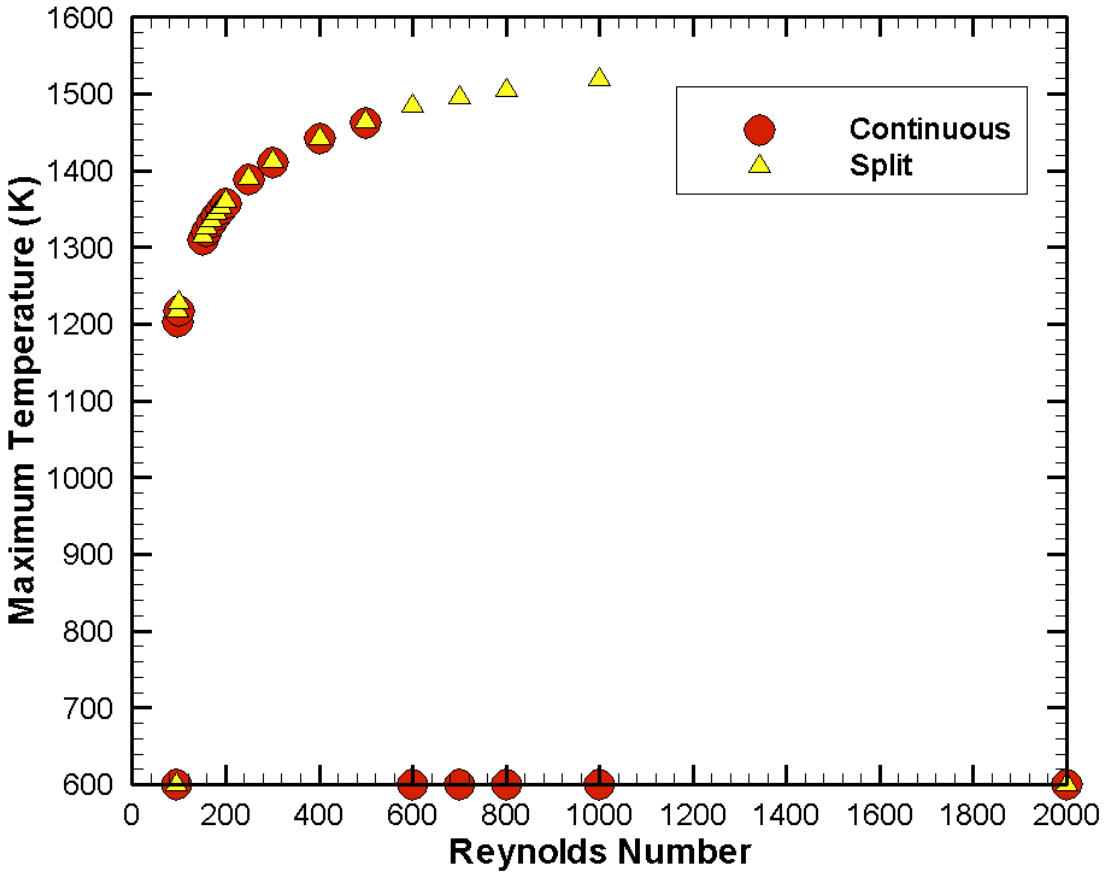

Figure 3.4: Maximum temperature characteristics for heterogeneous combustion of a stoichiometric (Φ = 1.0) methane-air mixture on platinum supported on a silicon carbide monolith with length 2L=5cm

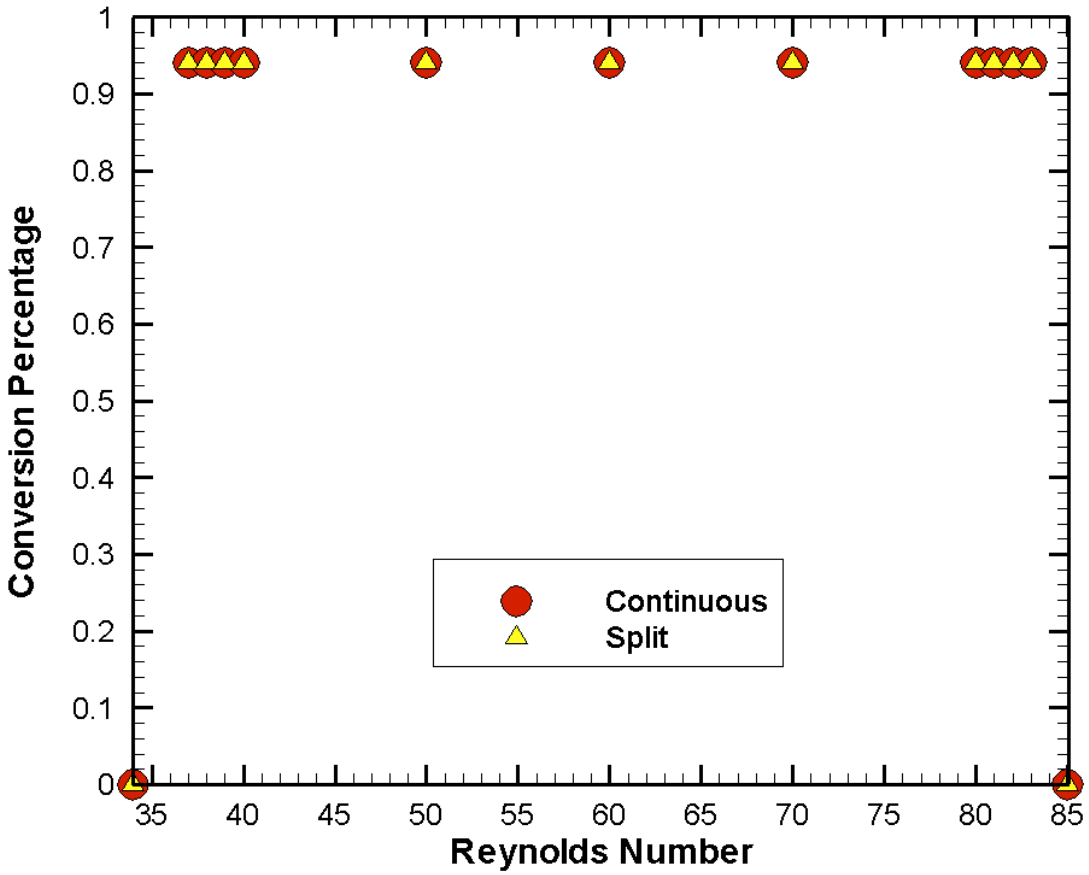

Figure 3.5: Ignition characteristics for heterogeneous combustion of a stoichiometric (Φ = 1.0) methane-air mixture on platinum supported on a cordierite monolith

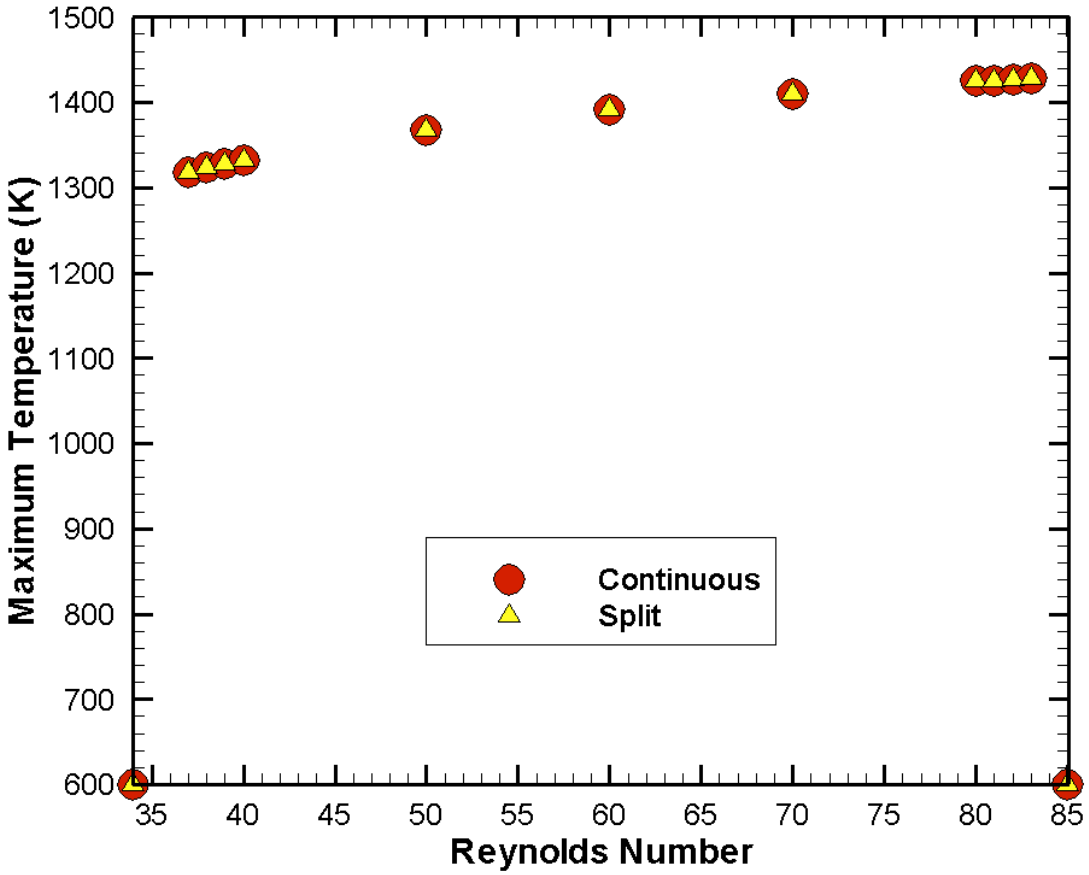

Figure 3.6: Maximum temperature characteristics for heterogeneous combustion of a stoichiometric (Φ = 1.0) methane-air mixture on platinum supported on a cordierite monolith

3.3 Effect of Monolith Splitting

For the silicon carbide stoichiometric cases at high Reynolds number, there was a large difference in blowout limits between the continuous and split tubes (Fig. 3.3, 3.4). While the continuous tube blew out at inlet flow Reynolds number 600, the split tube continued to ignite beyond a Reynolds number of 1000. When both the continuous and split tubes were igniting, e.g. at Reynolds number 300 (Fig. 3.7), their behavior is the nearly identical; they ignite, achieve steady state, and have approximately the same fuel conversion percentage and peak temperature. However, in a case where the split tube ignites and the continuous tube blows out, the simulation

results show the differing behavior is due solely to the air gap present in the split case. At Reynolds number 600, the simulation profiles of both the split and continuous cases taken at various instances in time during their ignition processes (Fig. 3.8) show that the continuous case is unable to sustain ignition while the split case ignition focuses upon the point of the air gap. The time-lapse temperature profile for the steady-state split tube (Fig. 3.8) shows that air gap hinders the propagation of thermal flow through the tube wall and forces the heat into the methane-air flow and thereby sustaining ignition. This conclusion is also apparent through the viewing of the steady-state methane fuel distribution (Fig. 3.9) and the steady-state exhaust production viewed as the carbon monoxide distribution (Fig. 3.10).

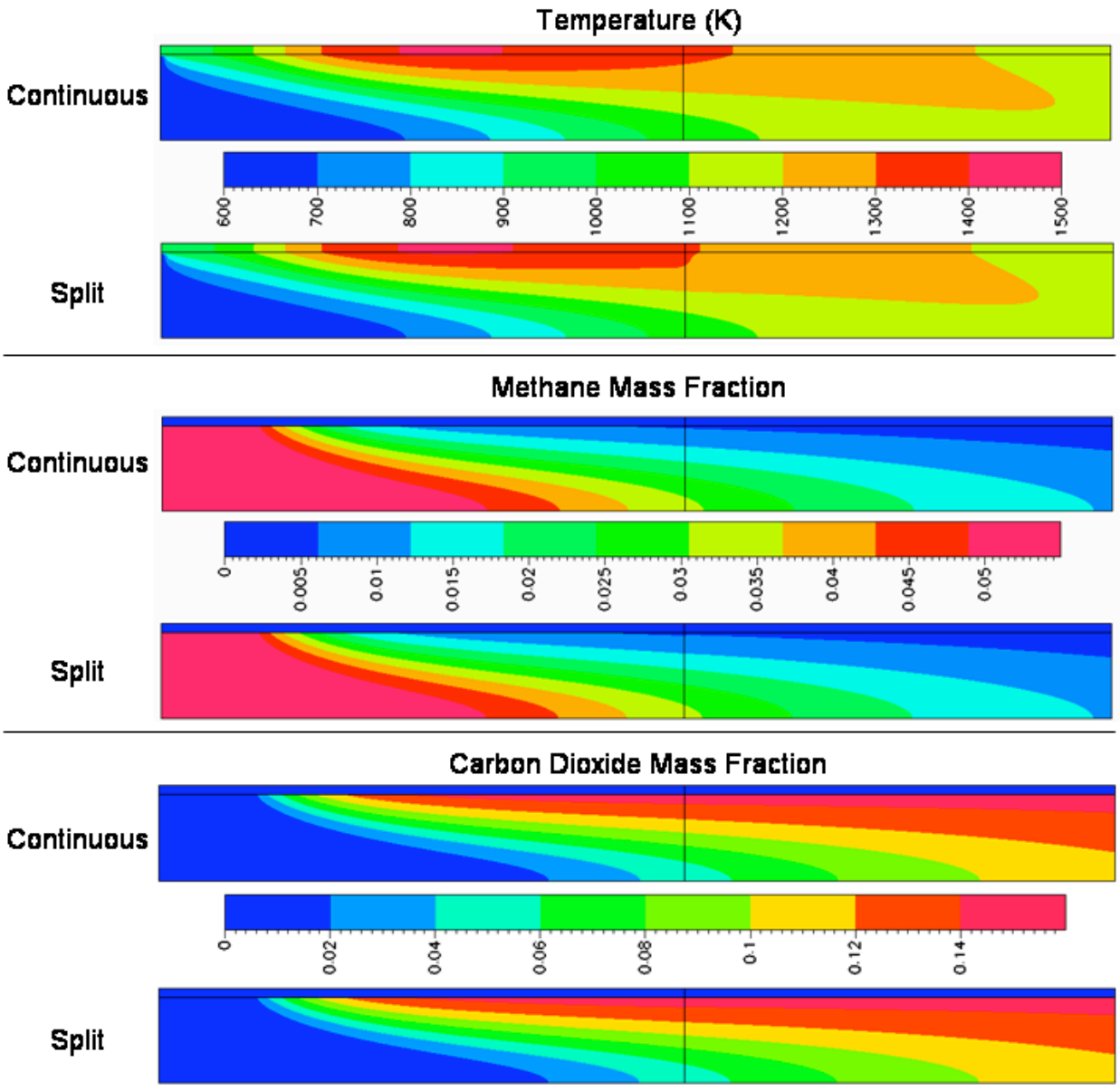

Figure 3.7: Split and continuous tubes heterogeneous combustion of a stoichiometric (Φ = 1.0) methane-air mixture on platinum supported on a silicon carbide monolith at steady state. Re = 300, length 2L=5cm

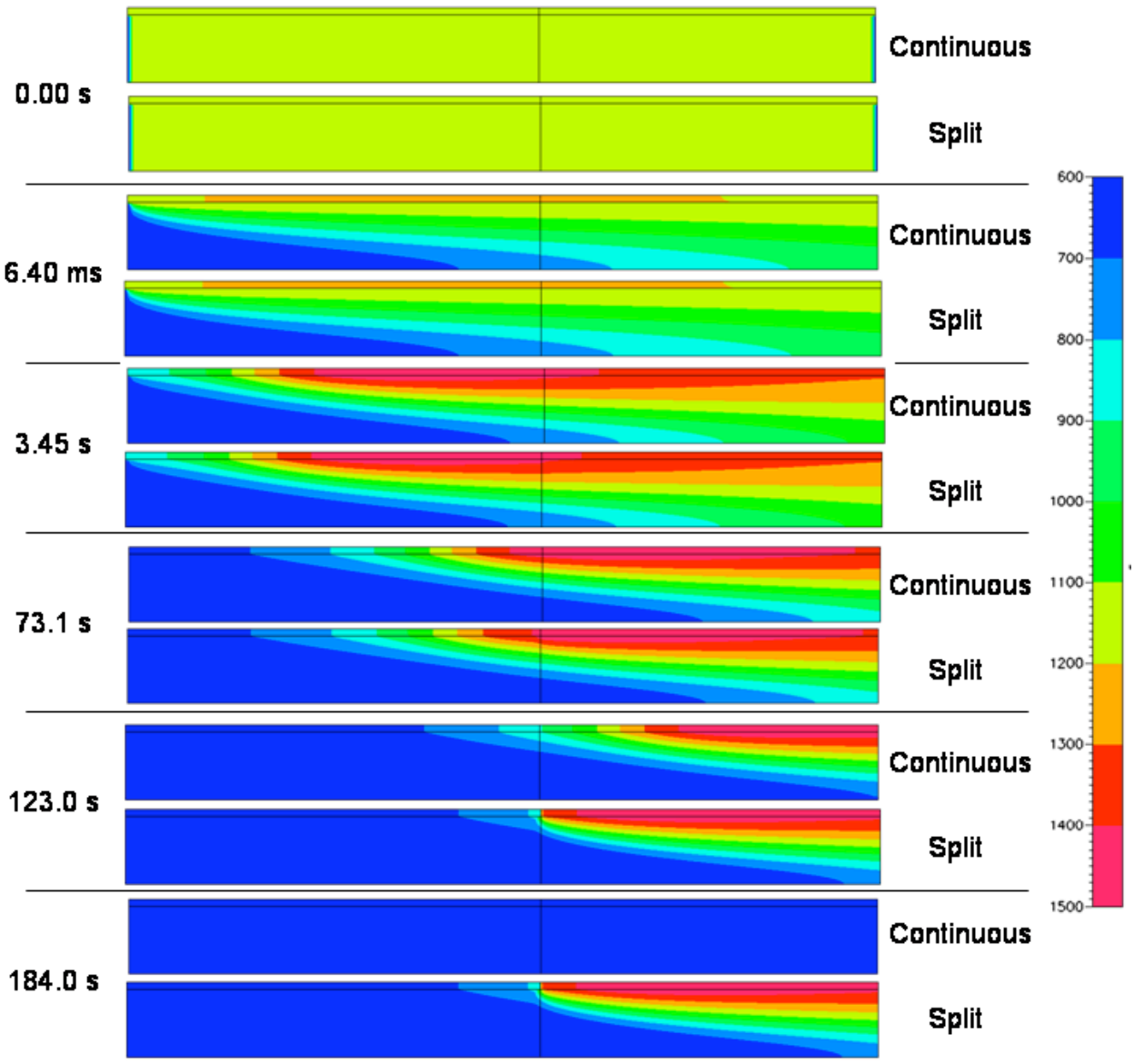

Figure 3.8: Comparison of temperature distribution between split and continuous silicon carbide monolith tubes from the onset of ignition to steady state. Heterogeneous combustion of a stoichiometric (Φ = 1.0) methane-air mixture on platinum supported on a silicon carbide monolith at Re = 60 with length 2L=5cm

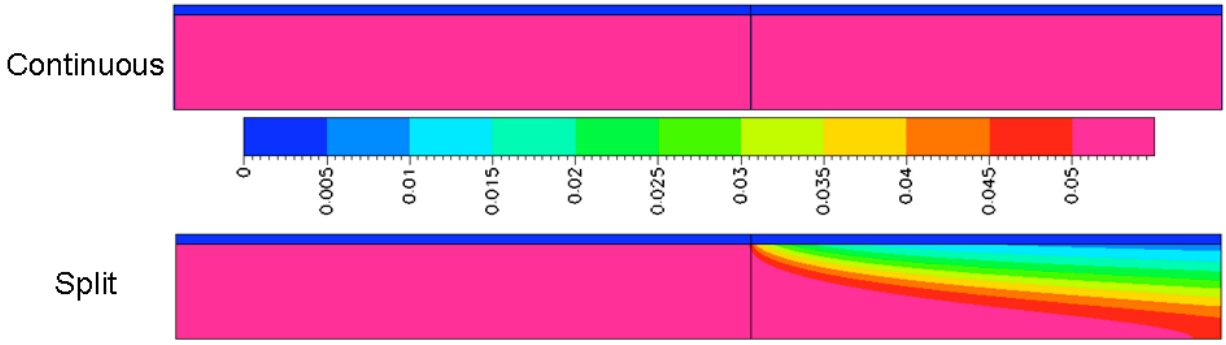

Figure 3.9: Comparison of methane distribution between split and continuous silicon carbide monolith tubes at steady state ignition from stoichiometric (Φ = 1.0) fuel. Re = 600, length 2L=5cm

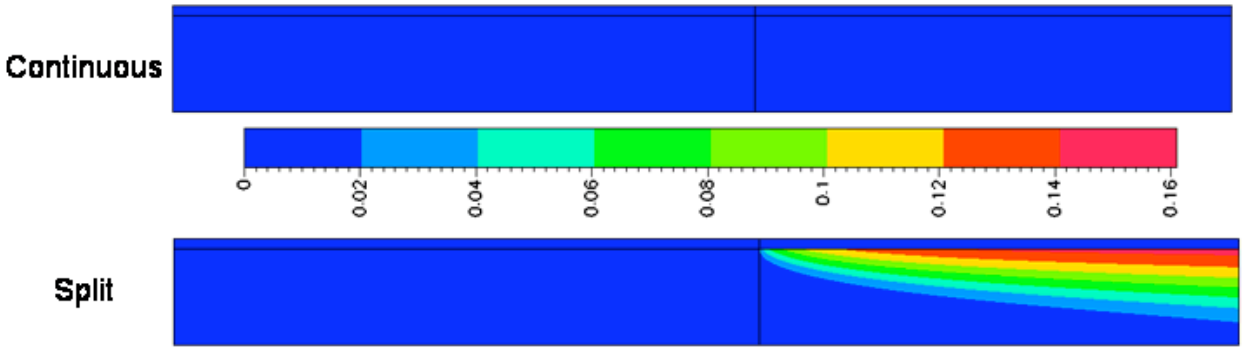

Figure 3.10: Comparison of carbon dioxide distribution between split and continuous silicon carbide monolith tubes at steady state ignition from stoichiometric (Φ = 1.0) fuel. Re = 600, length 2L=5cm

For the silicon carbide stoichiometric cases at low inlet flow velocity U_{in}, there are no significant differences between the ignition points of the continuous and split tubes (Fig. 3.3). Both simulations ignite at the same inlet Reynolds number and over the range of ignition achieve approximately the same conversion percentages and maximum temperatures (Fig. 3.3, 3.4). Therefore, for the silicon carbide stoichiometric cases at low inlet flow velocity, the conversion fractions are viewed as more or less independent of inlet flow speed at the low end of the range of Reynolds numbers simulated.

For the cordierite stoichiometric cases at all inlet flow velocities U_{in}, there are also no significant differences in the ignition and blowout points of the continuous and split tubes. As

with the silicon carbide tubes at low inlet velocities, the cordierite split and continuous cases have the same conversion percentages and maximum temperatures (Fig. 3.5, 3.6). However, the conversion percentage only varies by a small amount for the entire range of inlet flow velocities where ignition occurs, so the conversion fractions are viewed as more or less independent of inlet flow speeds simulated.

In the case of cordierite, no noticeable difference is observed between the split and the continuous tubes; both tubes ignite or blow out in a similar fashion. Additionally, once ignition occurs for the cordierite tube, the steady state conversion fraction is approximately 0.95 irrespective of the Reynolds number. In contrast, the split silicon carbide tube ignites over a much wider range of Reynolds number than the continuous case, and the conversion fraction decreases monotonically with increasing Reynolds number until blowout occurs. However, even for silicon carbide at low Reynolds numbers, the conversion fractions are more or less independent of Reynolds number.

It is clear from the above results that the effect of splitting the tube only manifests itself if the thermal conductivity of the tube material is high. Otherwise, wall heat conduction is weak to begin with (as in cordierite), and whether additional conduction resistance is imposed or not plays no role in the overall ignition and flame attachment process. One question that remains for the silicon carbide cases is why there is no difference in conversion fractions between split and continuous tubes at low-intermediate Reynolds number, while there is a large difference above a certain Reynolds number. To answer this question, temperature and mass fraction distributions were studied for a case where both tubes ignited (Fig. 3.7), where inlet flow speed is $Re_D = 300$. Comparison of the temperature distributions between the split and continuous tubes show observable differences in wall temperature, particularly near the splitting point. However, these

observable differences in temperature do not translate to observable differences in mass fraction of methane. Hence, the methane conversion fractions are similar. At low flow rates, the flame attachment point is close to the inlet and almost 85% of the methane gets consumed in the first tube section. Thus, any difference in wall temperature in the second half of the tube hardly has any effect on the overall conversion fraction. With increase in flow rate, the flame attachment point is expected to shift further downstream, in which case the effect of splitting the tube is expected to be amplified, as was already corroborated by the results shown in Figure 3.8 through snapshots obtained from transient simulations at different instances of time. These frames clearly show that the point of attachment of the flame in this case is in the second tube section. For the continuous monolith case, the heat is transferred downstream by axial conduction, and is eventually lost by both conduction and radiation to the relatively cold outlet. In the split monolith case, the heat is prevented from traveling downstream by the thermal resistance of the small air gap, and therefore cannot be dissipated as effectively. This facilitates attachment of the flame and enhances its stability at steady state, and is also confirmed in the methane and carbon monoxide distributions in Figures 3.9 and 3.10.

The results indicate that high thermal conductivity ceramic supports are more robust as design materials since they allow ignition and flame stability over a wider range of conditions while still achieving the same maximum temperature. The downside is that such materials may be susceptible to different behavior when the monolith is built with smaller building blocks as compared to continuous monolith tubes.

Chapter 4

SUMMARY AND CONCLUSIONS

Computational fluid dynamics calculations have been performed to elucidate key behavioral differences in heterogeneous combustion within continuous and split monolith tubes. Methane-air combustion on platinum is chosen as the candidate system, and a 24-step reaction mechanism is used to describe the surface chemistry. In the split tube case, two building blocks of length 2.5 cm each are used, and an air gap of 10 μm is introduced between the two blocks. Two commonly used ceramic materials, namely cordierite and silicon carbide are used for the supporting monolith material. Silicon carbide is representative of a material with high thermal conductivity, while cordierite is representative of a material with low thermal conductivity. Both materials have comparable thermal capacitance.

Simulation results showed that ignition occurs in cordierite tubes over a very narrow range of Reynolds number, ranging between 35 and 80. In contrast, ignition occurred in silicon carbide tubes in the range of Reynolds numbers between 20 and 1000, indicating that silicon carbide monoliths are likely to be much more robust and less susceptible in uncertainties in the Reynolds number. Therefore, monoliths composed of materials with high thermal conductivity values would be better candidates than monoliths created from materials with low thermal conductivity values. Within the narrow range of Reynolds numbers for which ignition occurred in cordierite tubes, it is observed that the steady state conversion fraction is virtually independent of the Reynolds number; in all cases, about 95% conversion was obtained. For silicon carbide, on the other hand, the conversion fraction decreased monotonically with increasing Reynolds number, until blowout occurred.

The difference in behavior between single and split monolith tubes manifested itself only for the high thermal conductivity material, namely silicon carbide. For cordierite, both tubes behaved almost identically. For silicon carbide, it was found that the introduction of a thin gap between the two sections of the tube reduced heat loss by axial conduction, facilitating attachment of the flame and subsequent steady state combustion. In the case of continuous tubes, even though ignition occurred, the flame could not be sustained due to rapid heat loss by axial conduction.

Chapter 5

FUTURE WORK

From an engineering perspective, the simulation results presented here can serve as guidelines for future design and troubleshooting of catalytic combustion processes. The work is easily extendable to other practical chemical systems, pending availability of reasonably accurate reaction mechanisms. This project could also be furthered through additional work in the construction and simulation of a full-scale model of a catalytic monolith. The major consideration for this model would be the availability of the computational resources (both time and memory) that would be necessary to solve the governing equations for the full monolith (as opposed to a single channel of the monolith). A successful simulation of the full monolithic catalytic converter would be useful in delineating the effects of flow and temperature non-uniformity within the monolith from channel to channel.

REFERENCES

Bird R.B., Stewart W.E., Lightfoot E.N. (2001), *Transport Phenomena*, Second ed., Wiley, New York.

Boehman, A.L., (1998), "Radiation Heat Transfer in Catalytic Monoliths," *AIChE Journal*, Vol. 44(12), pp. 2745-2755.

Choi, J,-S., Prikhodko, V., Chakravarthy, K., and Daw, S., (2006), "Assessing Monolith Length Effects on LNT Performance," *Ninth DOE Workshop on Lean Emissions Reduction Simulation*, May 2-4, Dearborn, Michigan, USA.

Coltrin, M., Kee, R.J., and Rupley, F., (1991) "Surface Chemkin: A General Formalism and Software for Analyzing Heterogeneous Chemical Kinetics at Gas-Solid Interfaces," *International Journal of Chemical Kinetics*, Vol. 23, pp. 1111-1128.

Desilets M., Proulx P., and Soucy G., (1997), "Modeling of multi-component diffusion in high temperature flows," *International Journal of Heat and Mass Transfer*, Vol. 40, pp. 4273-4278.

Deutschmann, O., Behrendt, F., and Warnatz, J., (1994), "Modeling and Simulation of Heterogeneous Oxidation of Methane on a Platinum Foil," *Catalysis Today*, Vol. 21, pp. 461-471.

Deutschmann, O., and Schmidt, L.D., (1998), "Modeling the Partial Oxidation of Methane in a Short Contact Time Reactor," *AIChE Journal*, Vol. 44, pp. 2465-2476.

Ertl, G., H. Knozinger, and J. Weitkamp. (1999) *Environmental Catalysis*. Wiley-VCH, New York.

Hayes, R.E., and Kolaczkowski, S.T., (1997), *Introduction to Catalytic Combustion*, Gordon and Breach Science Publishers.

Heywood, John B., (1988), *Internal Combustion Engine Fundamentals*, McGraw-Hill, Inc., New York.

Hirschfelder, J.O., Curtiss, C.F., and Bird, R.B., (1954) *Molecular Theory of Gases and Liquids*, Wiley, New York.

Kumar, A., and Mazumder, S., (2006), "Implications of the Dilute Approximation for the Prediction of Heat and Mass Transfer Rates in Multi-Component Systems," *Proceedings of the IMECE2006*, Paper No. IMECE2006-13113, Chicago, IL, November 2006.

Kumar, A., and Mazumder, S., (2007), "Assessment of Various Diffusion Models for the Prediction of Heterogeneous Combustion in Monolith Tubes," *Combustion Theory and Modelling*, submitted October 2006.

Kuo, K.K., (1986), *Principles of Combustion,* Wiley, New York.

Lynch, C.T. (editor), (1975), *CRC Handbook of Material Science, Volume III: Nonmetallic Materials and Applications*, CRC Press, Boca Raton, FL.

Mazumder, S. and Lowry, S.A, (2001), "The Treatment of Reacting Surfaces for Finite-Volume Schemes on Unstructured Meshes," *Journal of Computational Physics,* Vol. 173(2), pp. 512-526.

Mazumder, S. and Sengupta, D., (2002), "Subgrid Scale Modeling of Heterogeneous Chemical Reactions and Transport in Full-Scale Catalytic Converters," *Combustion and Flame*, Vol. 131(1-2), pp. 815.

Mazumder S., and Grimm, M., (2007), "Numerical Investigation of Participating Medium Radiation Effects in Catalytic Combustion," *Joint Summer ASME-JSME Heat Transfer Conference*, Vacouver, BC, Canada.

Modest M.F., (2003), *Radiative Heat Transfer*, Second Edition, Academic Press, San Diego, CA.

N.A.S.A., (1998), "It's a Clean Machine", *Spinoff 1998*, pp. 94-95, National Aeronautics and Space Administration, Office of Aeronautics and Space Transportation Technology, Commercial Programs Division.

Raja, L.L., Kee, R.J., Deutschmann, O., Warnatz, J., Schmidt, L.D., (2000), "A Critical Evaluation of Navier-Stokes, Boundary-Layer, and Plug-Flow Models for the Simulation of Flow and Chemistry in a Catalytic Combustion Honeycomb Channel," *Catalysis Today*, Vol. 59, pp. 47-60.

Ramesh, K.S., et al. (1997) *Catalyst Materials for High-Temperature Processes*. The American Ceramic Society, Westerville, OH.

Riedel, R. (Ed.), (2000), *Handbook of Ceramic Hard Materials*, Volume 2, Wiley-VCH, Chichester.

Song, X., William, W. R., Schmidt, L.D., and Aris, R., (1991), "Bifurcation behavior in homogeneous-heterogeneous combustion: II. Computations for stagnation-point flow," *Combustion and Flame*, Vol. 84, pp. 292-311.

Stutz, M.J., and Poulikakos, D., (2005), "Effects of microreactor wall heat conduction on the reforming process of methane," *Chemical Engineering Science*, Vol. 60, pp. 6983-6997.

Sutton K., and Knoffo P. A., (1998), "Multicomponent Diffusion with Application to Computational Aerothermodynamics," *AIAA paper number 98-2575.*

Wangard W., Dandy D.S., Miller B.J., (2001), "A Numerically Stable Method for Integration of the Multi-Component Species Diffusion Equations", *Journal of Computational Physics*, Vol. 174, pp. 460–472.